SATELLITE OBSERVATION OF CHANGES IN SUSPENDED SEDIMENT INDUCED BY A BAY BRIDGE

LiNa Cai[(1), (2), (3)], **DanLing Tang***[(1), (3)], **CongYing Li**[(4)]

[(1)] *Research Center for Remote Sensing of Marine Ecology & Environment, State Key Laboratory of Tropical Oceanography, South China Sea Institute of Oceanology, Chinese Academy of Sciences, Guangzhou 510301, China, *Email: lingzistdl@126.com*

[(2)] *Zhejiang Ocean University, Zhoushan Zhejiang 316004, China, Email: clnown@163.com*

[(3)] *University of Chinese Academy of Sciences, Beijing 100049, China*

[(4)] *Naval Aeronautical and Astronautical University, Yantai 264001, China, Email: yuanshanling@163.com*

ABSTRACT

Nearshore bridges may have impacts on ocean environments. This paper introduced how to investigate suspended sediment changes induced by a bay-bridge using remote sensing method. Hangzhou Bay Bridge (HBB) crossing Hangzhou Bay, in China, was taken as example. The spectral features of water were analyzed, and unsupervised classification of water quality was conducted, suspended sediment concentration (SSC) was inversed from Landsat TM data (30m spatial resolution) using a new established model. Those three aspects together revealed details of SSC changes induced by HBB. When water turbidity was low upstream, SSC increased 3% - 60% (8.4 mg·l^{-1}-176.29 mg·l^{-1}) downstream. In general, the more turbid the water in upstream, the less SSC increases amplitude downstream. If water turbidity was high (> 350 mg·l-1) upstream, SSC decrease can be observed in the range of 300 meters or further downstream from the bridge. It decreases nearly 2% -17.5% (12.6 mg·l-1-62.98 mg·l-1). This study shows that Landsat TM data and corresponding methods can display the changing patterns of SSC induced by a nearshore bridge in coastal waters.

Keywords: Remote sensing; Changes in suspended sediment; Influence of bridge; SS-CT

1. INTRODUCTION

Suspended sediment is one of the key factors of the ocean environment, it is a significant carrier of carbon, nutrients, pollutants and other materials [1-4]. The sediments of Hangzhou Bay are partly from the Yangtze River, which is the fourth largest sediment load river in the world with approximately more than 400 million tons per year [5, 6]. Suspended sediment influences the ecology, geomorphology evolution and water quality of Hangzhou Bay. Monitoring the behavior of suspended sediment is of great interest and importance.

Satellite data were used to track the suspended sediment concentration (SSC) in the coastal waters of China in the past [7, 8], and recently MODIS data were used to analyze the northward drift of SSC in the Yangtze estuary in spring [9]. The spatial resolution of most satellite data (such as SeaWiFS, MODIS, MERIS and GOCI) is relatively low, of the order of a few hundred meters. Such data are too sparse to estimate the effects of bridges on the local ocean sedimentary environment. Therefore, remote sensing data with higher spatial resolution are needed. Till now, the method of remote sensing of SSC variation induced by crossing bay bridge is still under developing.

In this paper, we analyzed the spectral features of turbid waters, conducted unsupervised classification using Landsat Thematic Mapper (TM) data and estimated the SSC around the bridge from TM images. We aim to determine how to apply satellite data to observe variation of suspended sediment concentration patterns in the vicinity of Hangzhou Bay Bridge (HBB) in the Hangzhou Bay, East China Sea.

2. DATA AND METHOD

2.1. Study Area and Hangzhou Bay Bridge

Hangzhou Bay is located in the East China Sea, between 29°-32° N and 120°-123° E (Fig.1 a, b) with an area of approximately 8500 km^2. Its average depth at low tide is 8-10 m [10-12].

The Hangzhou Bay Bridge (Fig. 1c and d) is a large bridge with a length of about 36 km spaning the main channel of the bay. It was built in 2003 and has been operating since 2007.

2.2. In Situ Field Data Collection

In order to determine the spectral feature of the SSC in Hangzhou Bay, we analyzed in situ spectral data. The survey was conducted in Hangzhou Bay (yellow square in Fig. 1, b) in 2009 and 2014 using an ISI921VF visible, near-infrared (NIR), high spectral radiometer with 380-1080 nm spectral range. The remote sensing reflectance (Rrs) together with SSC were synchronously measured.

Proc. 'Dragon 3 Mid-Term Results Symposium', Chengdu, P.R. China
26–29 May 2014 (ESA SP-724, November 2014)

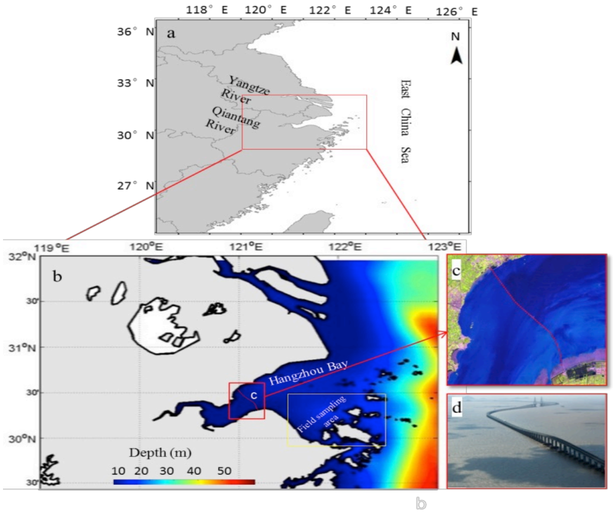

Figure 1. Location of the study area (a: Location of Hangzhou Bay; b: Bathymetry Information of Hangzhou Bay; c: False Color Image Composited from TM Bands 5, 4 and 3; Red Curve in c: HBB; d: Photo of HBB)

2.3. Analysis of Landsat-5 TM Data

Landsat-5 TM images were chosen to analyze the changes in SSC. The wavelength used in the TM sensor was from 0.45 µm to 12.50 µm and seven spectral bands were defined. The spatial resolution is 30 m for the visible, NIR bands and short wave infrared bands, 120 m for the thermal infrared band [13]. Seven Landsat- 5 TM images in clear sky were acquired at around 10:15 (a.m.) on Jul. 2, 2007; Jul. 28, 2007; Mar. 24, 2008; May 11, 2008; Jul. 17, 2009; Nov. 9, 2010; Jul. 23, 2011, respectively.

In this paper, we conducted the atmospheric correction by using a dark pixel subtraction method [14-16]. To convert the digital data to radiance at the sensor, the calibration was carried out using the formula of Onderka and Pekárová [17] and listed in Eq. (1):

$$L_\lambda = Bias_\lambda + Gain_\lambda \times DN_\lambda \tag{1}$$

L_λ: the radiance in units of W/(m^2 sr µm),

$Bias_\lambda$ and $Gain_\lambda$: the bias [Wm^{-2} sr^{-1} µm^{-1}] and gains [Wm^{-2} sr^{-1} µm^{-1}] for the λ wavelength band,

DN_λ: the digital number [18, 17].

In order to investigate the difference in water quality near the bridge, unsupervised classification and spectral profile curve analysis were performed. In this paper, we adopted the ISODATA (Iterative Self-Organizing Data Analysis Techniques Algorithm) to perform the unsupervised classification [19-21].

To clearly analysis the variation of SSC induced by the HBB, SSC was retrieved from Landsat-5 TM data using a new established model. Furthermore, SSC comparative analysis was conducted from sampling paired sub-areas and paired points on opposite side of the bridge.

3. RESULTS

3.1. Water Spectral Profile Curves and Classes on Two Sides of The Bridge

Two-dimensional spectral feature spaces have been retrieved from the TM image on July 28, 2007 (bands 1 and 3, 1 and 4, 2 and 4 were taken as examples). The candle light shaped part in white circles represents sea water. The pixels of the same water quality have the same pixel value in every band and cluster together in the same place (Fig. 2(a-c)). The different positions in the white circled areas represent different levels of water quality.

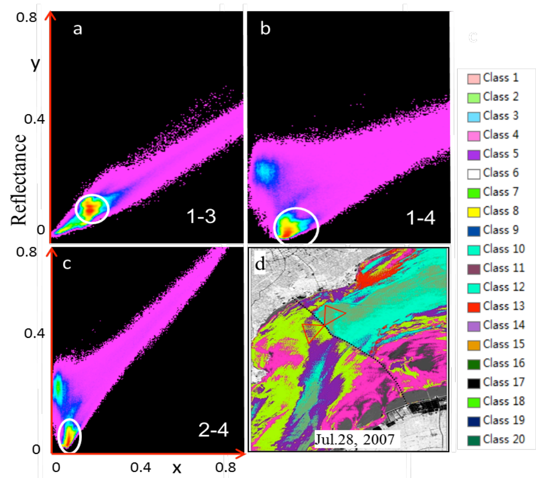

Figure 2. (a-c) Two-Dimensional Spectral Feature Space of Every Two Bands (Arabic Numerals in Each Block: Band Number that Comprise the Spectral Feature Space; First Band Number: x Axis; Second Number: y Axis). (d) Results of Water Unsupervised Classification Derived from Landsat-5 TM Images (Black Dotted Line: HBB)

Based on the spectral feature space from the Landsat TM multispectral image, sea water of study area can be separated into 20 classes (Fig.2d). An obvious difference in water class was observed on the opposite sides of the bridge, which has been highlighted by red triangles in Fig. 2(d).

Different patterns of water classes, indicating different optical characteristics. In situ data got from Hangzhou Bay was sampled to analyze the relationship between SSC and each spectral band. As was shown in

Fig.3 that two reflectance peaks were found in the measurement of spectral curves, with the first being around 700 nm, and the second being around 800 nm. The intensity of two peaks is close. The reflectance in the red and NIR bands increases with the increase of SSC.

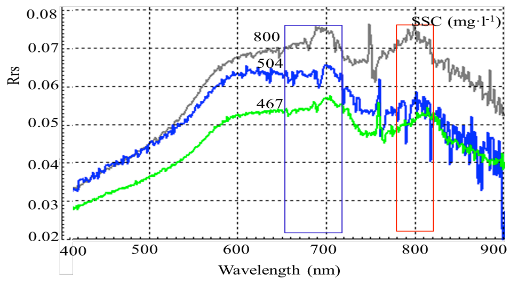

Figure 3. Spectral Reflectance Curves of Sampling Points in Hangzhou Bay

Spectral curves and values were obviously different on opposite sides of HBB (Fig. 4(A1-C1)), this is especially the case in the red and NIR bands (red dotted line frames in Fig. 4(A1-C1)). The water leaving reflectance on the downstream side of the HBB changed, becoming larger or smaller than those on the upstream side.

3.2 Estimation of SSC Model

The calibration data set contained 23 water samples, with SSC values ranging from 263.6 to 473.2 $mg{\cdot}l^{-1}$ with a mean value of 361.52 $mg{\cdot}l^{-1}$. Water spectral analysis and correlation analysis were carried out to determine the relationship between the SSC and reflectance as a function of wavelength. The estimation model of SSC was built based on regression Eq. (2):

$$SSC = ai * xi + b + \varepsilon \quad (2)$$

Where x is the calibrated radiance in a corresponding band, ai are the coefficients, b is the intercept (constant) of a linear regression, ε is a random error, i can be one for a single band or more for a combination (multiple regression).

The linear correlation between SSC and Rrs at different wavelengths was analyzed in Tab. 4. Near infrared band indicates the highest correlation between SSC and Rrs compared with blue, green and red bands, with the correlation coefficient R 0.841 (averaged from 765nm and 865nm). The red band presents a secondary peak in the correlation with the SSC, with R 0.713. Therefore, the near infrared band (TM4) and the red band (TM3) can be adopted to establish estimation model of SSC. The new model is named as SS-CT (Eq. (3)):

$$SSC = 6.219 * (0.327 * L3 + 0.673 * L4) - 251.962 \quad (3)$$

Where SSC is the suspended sediment concentration (mg·l-1), L3, L4 are the calibrated radiance in the red band (TM3) and near-infrared band (TM4). The factoring of Eq. (3) represents a weighted sum of bands combination with the red band weight of 0.327 and near-infrared band weight of 0.673. This combination shows the best correlation (R 0.956 and $P<0.005$) with SSC than other weight assignment and was confirmed by an independent iterative weight analysis among 1000 weight assignments.

The calculation were performed with software ENVI 4.5 [22].

Table 1. Eigenvalues of linear regression between SSC and the Rrs at different wavelengths

Wavelength a (nm)	SSC				
	R	R^2	$\overline{R}^2$	Sig (P)	F
443B	0.643	0.413	0.364	0.013	8.439
510 B	0.556	0.310	0.252	0.039	5.379
555 G	0.552	0.304	0.246	0.041	5.247
660 G	0.707	0.499	0.452	0.005	11.975
670 R	0.710	0.505	0.463	0.004	12.226
680 R	0.716	0.513	0.472	0.004	12.644
765 N	0.834	0.696	0.671	0.000	27.503
865 N	0.847	0.717	0.693	0.000	30.39

a B-Blue, G-Green, R-Red, N-Near infrared

3.3 SS-CT Retrieved SSC

3.3.1 Variation of SSC in The Vicinity of The Bridge

Distributions of the SSC (Fig. 4) in the research area have been retrieved from TM images (taken on July 28, 2007; July 17, 2009; July 23, 2011 as examples). In this paper, two sides of the bridge, the upstream (UP) and downstream (DW) were defined according to the pier induced flow (pier wake) and the position relative to the bridge. The pier induced flow can be interpreted from Landsat-5 TM enhanced color images (Fig. 4(D)). We define the pier wake side as downstream, and the opposite side of the bridge as upstream.

The SSC on the northwest and south of the bridge was higher than that near the center of the bridge (Fig. 4(A2-C2)). Along HBB from north to south, SSC changed obviously, with the lowest in the middle the highest in the south, and the moderate concentrations in the north. The maximum SSC in study area was nearly 750 mg·l^{-1} with the average SSC being around 300 mg·l^{-1}. These levels showed that water in the research area is high turbidity. In addition, distinctly different distributions of SSC were observed on opposite sides of the bridge.

Comparisons between in situ SSC and SS-CT values showed a close agreement (Fig. 5a) with a highly significant linear relationship with an R of 0.986, R^2 971, F 1253.819, P <0.005. The SS-CT mode is suitable for single image comparison of SSC between two sides of the bridge.

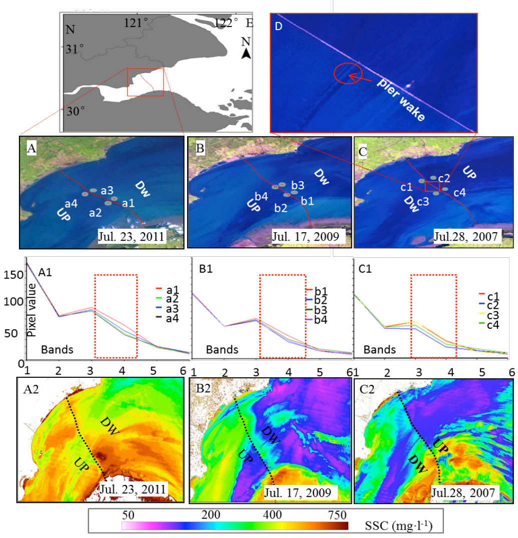

Figure 4. Comparison of Spectral Profile Curves Between Paired Sampling Points (a1-a4, b1-b4, c1-c4: Sampling Points in A-C and Corresponding Spectral Profile Curves in A-C1; D: Bridge Pier Wake.) Surface SSC Derived from Landsat TM Images (A2-C2: SSC on July 23, 2011, July 17, 2009 and July 28, 2007; Black Dotted Line: HBB; A and B: Histogram of Each Corresponding Sub- Area in Sub-figure b.)

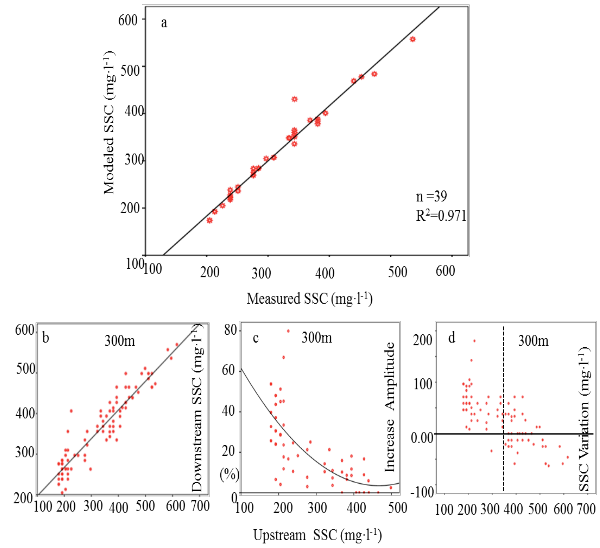

Figure 5. Comparison of the measured SSC and estimated SSC from SS-CT model (a). (b) Regression analysis of upstream water SSC and downstream SSC sampled 300 m downstream(c). (c) Regression analysis of upstream water SSC and downstream SSC increase amplitude in the range 300 m downstream. (d) Scatter plot for upstream water SSC and downstream water SSC variation; the points of unchanged SSC distribute on horizontal line, positive value denotes SSC increase and negative value denotes SSC decrease.

3.3.2 SSC on Two Sides of The Bridge

The SSC of upstream sub-area A was clearly lower than that of downstream sub-area B (Fig. 6, Tab. 2), with the mean values 177 mgl^{-1} and 253 mg·l^{-1} respectively. The same result was also observed across sampled pairs I and J, with the mean SSC values of 351 mg·l^{-1} and 433 mg·l^{-1}. The SSC increase amplitude were 76 mg·l^{-1} and 82 mg·l^{-1} from upstream to downstream. However, SSC decline phenomenon was observed in some paired sub-areas. For example, the decrease in amplitude of the SSC across upstream samples D, F and H compared to their downstream pairs C, E and G were 6 mg·l^{-1}, 43 mg/l and 35 mg·l^{-1}, respectively (Tab. 2).

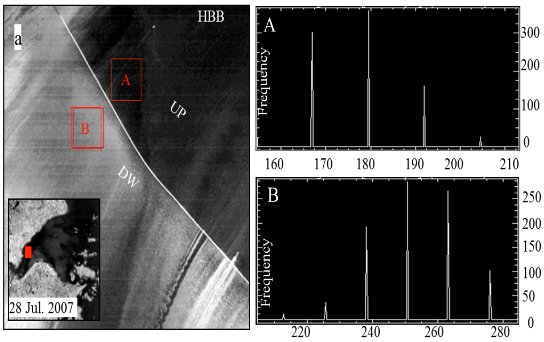

Figure 6. Comparisons of the SSC in the sampling sub-areas between upstream and downstream. (a) Inversed SSC map. Red boxes: sampling sub-areas. (A-B in red boxes) Upstream sampled sub-area and downstream sampled sub-area. (A-B in right hand side) Histogram of each corresponding sampling area.

Table 2. Basic statistics of SSC (mg·l^{-1}) in sampling sub-areas (Fig. 5)

Sub-area	Min	Max	Mean	Variation		Std dev
A	154	213	177 (UP)			11.48
B	204	284	253 (DW)	76 ↑	42.9% ↑	14.27
C	225	322	286 (UP)			15.94
D	238	309	280 (DW)	6 ↓	2.1% ↓	9.13
E	381	427	404 (UP)			7.5
F	322	406	361 (DW)	43 ↓	10.6% ↓	14.42
G	439	511	473 (UP)			10.92
H	414	473	438 (DW)	35 ↓	7.4% ↓	8.81
I	322	406	351 (UP)			16.61
J	355	498	433 (DW)	82 ↑	23.4% ↑	27.16

One hundred paired points, one point sampled upstream just close to the bridge and its pair sampled downstream along the streamline in the range of 300 meters from the bridge, were selected on TM images. These one hundred paired points were evenly sampled from different SSC water in study area.

The comparison of SSC showed that in the vicinity of HBB can change significantly on opposite sides of the bridge. When water turbidity was low upstream, SSC tends to increase downstream (Fig. 5d). In general, the more turbid the water in upstream, the less SSC increases amplitude downstream (Fig. 5c). If water turbidity was high (> 350 mg·l^{-1}) upstream, SSC decrease can be observed in the range of 300 meters or further downstream from the bridge (Fig. 5d).

4. DISCUSSION

4.1. SSC Sensitive Spectral Bands

Water spectral characteristics in Hangzhou Bay from a previous study [11] and in situ measurements (Fig. 2) were consistent with the measurement results from the Yellow River Estuary [23]. They showed the typical spectra characteristics of high turbidity water seen in other studies [24-26]. Water surface reflectance of the study areas in Hangzhou Bay are also dominated by the SSC [11, 26].

The spectral curves show clearly that the reflectance in the red and NIR bands correspond well to high SSC water (Fig. 2, Fig. 4 and Fig. 5). So the difference of water spectral profile curves from Landsat TM images of Hangzhou Bay in the red and NIR bands on opposite sides of the bridge are mainly induced by the changes in SSC.

4.2. Effectiveness of SSC Inversion

Based on the analysis above, red and near-infrared band can be adopted as the main band for establishing surface water SSC remote-sensing inversion model in Hangzhou Bay. The distribution of inversed SSC found in this study (taken for example on July 28, 2007) is consistent with the SSC inversion results in previous research [18]. Therefore, the inversed result can be used to conduct SSC comparison between two sided of the bridge in every single image of Hangzhou Bay.

4.3. The Evidence of SSC Differences on Opposite Sides of HBB

The first evidence is the difference in spectral profile and water classes on opposite sides of the bridge. The difference in the water spectral profile curves in the red and NIR bands on opposite sides of the bridge is mainly induced by SSC (Fig. 4). Therefore, the difference in classes on opposite sides of the bridge and the phenomenon of the bridge isolating the water body can indicate a distinct difference in the SSC (Fig. 3d).

The second and direct evidence is SSC inversion results. The distribution of SSC (Fig. 4(A2-C2)) suggests an obvious change in the SSC between the upstream and downstream sides of the bridge. The bridge appears to be a line of separation interrupting the sediment transport and leading to SSC differences on opposite sides of the bridge.

CONCLUSIONS

Landsat TM images can be used to investigate the impacts of a bridge on local ocean environments. It is appropriate to use TM3 and TM4 to inverse the SSC in the bay area. Three aspects (Fig. 7A), unsupervised classification, the spectral feature analysis and the inversion of SSC, together can display very well the SSC changes induced by crossing bay bridge in Hangzhou Bay. These changes indicate that the bridge can induce the change of sediment transport.

The variations of SSC in vicinity of the bridge from upstream to downstream are significant. Under the condition of low turbidity in upstream water, the SSC tends to increase in downstream side; however, for high turbidity in upstream water, the SSC tends to decrease downstream (Fig. 7B).

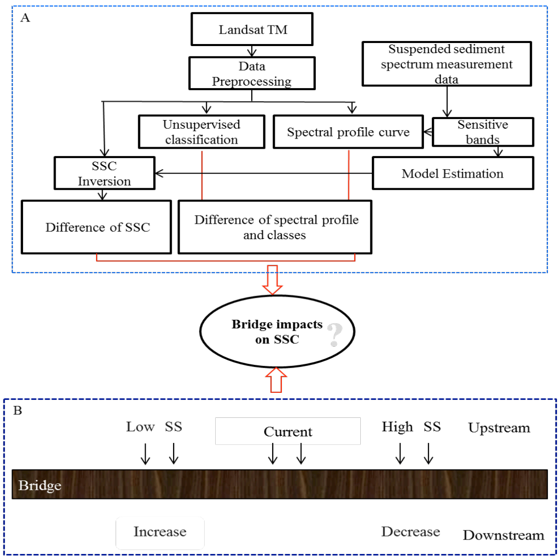

Figure 7. Remote sensing method and mechanism of bridge impacts on SSC nearby.

ACKNOWLEDGEMENTS

This work is jointly supported by research projects awarded to D.L. Tang: (1) Key Project of National Natural Sciences Foundation of China （NNSFC）; (2) Dragon 3 Project of ESA and NRSCC (Tang & Alpers, Project10705); (3) Group Program of State Key Laboratory of Tropical Oceanography (LTOZZ-1201). This work is also supported by research project of Zhejiang education department (Y201225122). The Center for Earth Observation and Digital Earth, Chinese Academy of Sciences provided Landsat-5 TM data.

REFERENCES

1. Ilyina, T., T. Pohlmann, G. Lammel &J. Sündermann. (2006). A Fate and Transport Ocean Model for Persistent Organic Pollutants and Its Application to the North Sea. *Journal of Marine Systems*. **63**(1), 1-19.
2. Mayer, L.M., R.G. Keil, S.A. Macko, S.B. Joye, K.C. Ruttenberg &R.C. Aller. (1998). Importance of Suspended Participates in Riverine Delivery of Bioavailable Nitrogen to Coastal Zones. *Global Biogeochemical Cycles*. **12**(4), 573-579.
3. Webster, T.&C. Lemckert. (2002). Sediment Resuspension within a Microtidal Estuary/Embayment and the Implication to Channel Management. *Journal of Coastal Research*. **36**, 753-759.
4. Yan, Z.&D.L. Tang. (2009). Changes in Suspended Sediments Associated with 2004 Indian Ocean Tsunami. *Advances in Space Research*. **43**(1), 89-95.
5. Chen, S.L., G. Zhang &S. Yang. (2003). Temporal and Spatial Changes of Suspended Sediment Concentration and Resuspension in the Yangtze River Estuary. *Journal of Geographical Sciences*. **13**(4), 498-506.
6. Milliman, J.D.&K.L. Farnsworth. (2011). *River Discharge to the Coastal Ocean: A Global Synthesis*.
7. Shen, F., W. Verhoef, Y. Zhou, M.S. Salama &X. Liu. (2010). Satellite Estimates of Wide-Range Suspended Sediment Concentrations in Changjiang (Yangtze) Estuary Using Meris Data. *Estuaries and coasts*. **33**(6), 1420-1429.
8. Tang, D.L., I. Ni, F. Müller-Karger &Z. Liu. (1998). Analysis of Annual and Spatial Patterns of Czcs-Derived Pigment Concentration on the Continental Shelf of China. *Continental Shelf Research*. **18**(12), 1493-1515.

9. Zhang, X.F., F. Hu, J. Zhang &D.L. Tang. (2014). Northward Drift of Suspended Sediment Concentration in the Yangtze Estuary in Spring. *International Journal of Remote Sensing*. **35**(11-12), 4114-4126.
10. Liu, S., Y. Liu, G. Yang, S. Qiao, C. Li, Z. Zhu &X. Shi. (2012). Distribution of Major and Trace Elements in Surface Sediments of Hangzhou Bay in China. *Acta Oceanologica Sinica*. **31**(4), 89-100.
11. Wang, F., B. Zhou, X. Liu, G. Zhou &K. Zhao. (2012). Remote-Sensing Inversion Model of Surface Water Suspended Sediment Concentration Based on in Situ Measured Spectrum in Hangzhou Bay, China. *Environmental Earth Sciences*. **67**(6), 1669-1677.
12. Xie, D., Z. Wang, S. Gao &H. De Vriend. (2009). Modeling the Tidal Channel Morphodynamics in a Macro-Tidal Embayment, Hangzhou Bay, China. *Continental Shelf Research*. **29**(15), 1757-1767.
13. Zhou, W., S. Wang, Y. Zhou &A. Troy. (2006). Mapping the Concentrations of Total Suspended Matter in Lake Taihu, China, Using Landsat - 5 Tm Data. *International Journal of Remote Sensing*. **27**(6), 1177-1191.
14. Chavez Jr, P.S. (1988). An Improved Dark-Object Subtraction Technique for Atmospheric Scattering Correction of Multispectral Data. *Remote sensing of environment*. **24**(3), 459-479.
15. Pattiaratchi, C., P. Lavery, A. Wyllie &P. Hick. (1994). Estimates of Water Quality in Coastal Waters Using Multi-Date Landsat Thematic Mapper Data. *International Journal of Remote Sensing*. **15**(8), 1571-1584.
16. Warrick*, J., L. Mertes, D. Siegel &C. Mackenzie. (2004). Estimating Suspended Sediment Concentrations in Turbid Coastal Waters of the Santa Barbara Channel with Seawifs. *International Journal of Remote Sensing*. **25**(10), 1995-2002.
17. Onderka, M.&P. Pekárová. (2008). Retrieval of Suspended Particulate Matter Concentrations in the Danube River from Landsat Etm Data. *Science of the total environment*. **397**(1), 238-243.
18. Li, J., S. Gao &Y. Wang. (2010). Delineating Suspended Sediment Concentration Patterns in Surface Waters of the Changjiang Estuary by Remote Sensing Analysis. *Acta Oceanologica Sinica*. **29**(4), 38-47.
19. Ball, G.H.&D.J. Hall. (1965). *Isodata, a Novel Method of Data Analysis and Pattern Classification*. DTIC Document.
20. Irvin, B.J., S.J. Ventura &B.K. Slater. (1997). Fuzzy and Isodata Classification of Landform Elements from Digital Terrain Data in Pleasant Valley, Wisconsin. *Geoderma*. **77**(2), 137-154.
21. Li, L., Q. Jiang, L. Zhang, G. Ding, L. Wang, R. Zhang, Z.G. Zhang, Q. Li, J.R. Ewing &A. Kapke. (2006). Ischemic Cerebral Tissue Response to Subventricular Zone Cell Transplantation Measured by Iterative Self-Organizing Data Analysis Technique Algorithm. *Journal of Cerebral Blood Flow & Metabolism*. **26**(11), 1366-1377.
22. ENVI. (1997). Envi User's Guide. *Research Systems Inc*, Chapter 1-10.
23. Qiu, Z.F. (2013). A Simple Optical Model to Estimate Suspended Particulate Matter in Yellow River Estuary. *Optics Express*. **21**(23), 27891-27904.
24. Curran, P.&E. Novo. (1988). The Relationship between Suspended Sediment Concentration and Remotely Sensed Spectral Radiance: A Review. *Journal of Coastal Research*. **4**(3), 351-368.
25. Doxaran, D., N. Cherukuru &S.J. Lavender. (2006). Apparent and Inherent Optical Properties of Turbid Estuarine Waters: Measurements, Empirical Quantification Relationships, and Modeling. *Applied Optics*. **45**(10), 2310-2324.
26. Zhang, M., J. Tang, Q. Dong, Q. Song &J. Ding. (2010). Retrieval of Total Suspended Matter Concentration in the Yellow and East China Seas from Modis Imagery. *Remote Sensing of Environment*. **114**(2), 392-403.